Volume 16
Number 21
7 June 2025
Pages 9033–9544

Chemical Science

rsc.li/chemical-science

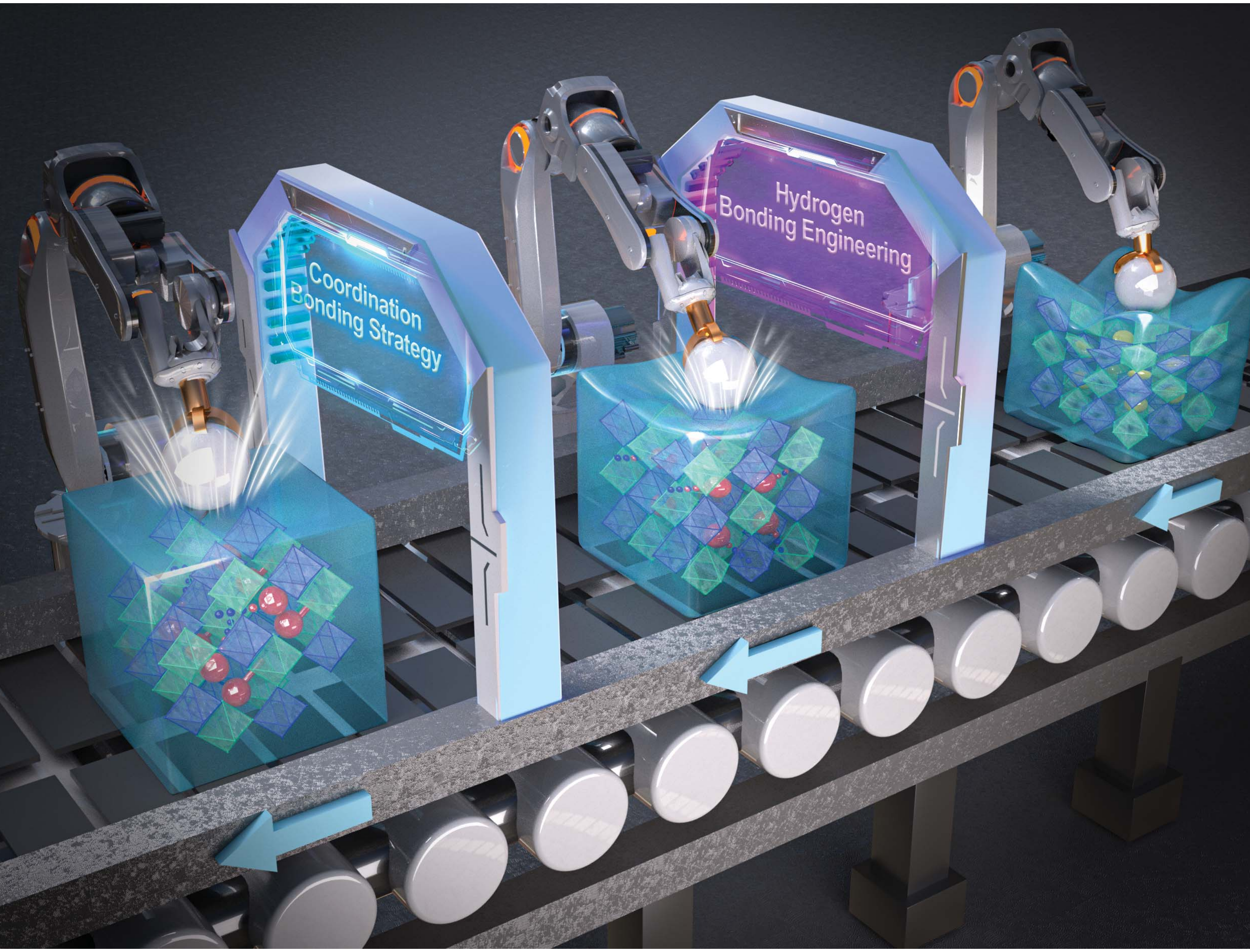

ISSN 2041-6539

ROYAL SOCIETY OF CHEMISTRY

EDGE ARTICLE
Yan Qin, Xiao-Gang Chen *et al.*
Giant mechanical tunability by a coordination bond strategy in a 3D hybrid cyanide double perovskite ferroelastic with reconstructive phase transition

15 YEARS ANNIVERSARY

Chemical
Science

ROYAL SOCIETY
OF CHEMISTRY

EDGE ARTICLE

View Article Online
View Journal | View Issue

Cite this: *Chem. Sci.*, 2025, **16**, 9109

All publication charges for this article have been paid for by the Royal Society of Chemistry

Giant mechanical tunability by a coordination bond strategy in a 3D hybrid cyanide double perovskite ferroelastic with reconstructive phase transition†

Hui-Peng Lv,‡ Sheng-Qian Hu,‡ Yong-Ju Bai, Jun-Si Zhou, Luan-Ying Ji,
Zhong-Xia Wang, Yong Ai, Yan Qin* and Xiao-Gang Chen*

Three-dimensional (3D) cyanide hybrid organic–inorganic double perovskites (CHOIPs) have abundant electrical, optical, thermal, and magnetic properties due to their diverse chemical variability and structural flexibility, making them promising for applications in transducers, memories, and switch materials. However, the mechanical properties, crucial for practical applications, have long been overlooked. Here, we present a substantial improvement in the mechanical strength of a 3D CHOIP using the coordination bond strategy. Through introducing the hydroxyl group into the parent compound $(CH_3CH_2NH_3)_2[KFe(CN)_6]$ (EA), two isomeric $(HOCH_2CH_2NH_3)_2[KFe(CN)_6]$ (EAOH-1 and EAOH-2) materials that both crystallized in the $P2_1/n$ space group at room temperature can be obtained. Notably, EAOH-1, featuring C–O–K coordination bonds between organic cations and the $[KFe(CN)_6]^{2-}$ framework, exhibits a nearly 300% increase in the elastic modulus (E) and hardness (H) compared to EA. In contrast, EAOH-2, which relies on weak 1D hydrogen bond interactions, shows approximate enhancements of 140% in E and 50% in H over EA. More interestingly, the significant decreases in both E and H induced by the thermally induced reconstructive phase transition from EAOH-1 to EAOH-2 further demonstrate the significant effect of the coordination bond strategy on the mechanical properties. This study highlights the potential of the coordination bond strategy to enhance the mechanical properties of CHOIPs, paving the way for the design of advanced materials with tailored mechanical performance.

Received 23rd January 2025
Accepted 18th April 2025

DOI: 10.1039/d5sc00620a

rsc.li/chemical-science

Introduction

Three-dimensional (3D) cyanide hybrid organic–inorganic double perovskites (CHOIPs) are compounds with the general formula $A_2B^IB^{III}X_6$, where the X-site is a cyanide group (CN^-), the B-site consists of mixed monovalent and trivalent metals, and the A-site contains organic cations. The CN^- group can be connected to different metals at both ends, making it an ideal X-site that forms a cubic skeleton with mixed metals to accommodate organic cations.[1,2] In 3D CHOIPs, symmetry changes could be driven by the individual or synergistic effect of the tilt or distortion of the cubic framework, the displacement of metal ions, and the order–disorder transition and/or displacement of organic cations, thus leading to the phase transition process. These complex phase transition dynamics endow CHOIPs with rich physical properties, such as ferroelectricity,[3–6] ferroelasticity,[6–13] dielectric switches,[6–12,14–18] second harmonic effects,[3] third-harmonic generation switching,[18] *etc.*, and thus have promising application prospects in the fields of nonvolatile memories, transducers, microelectronic switches, and nonlinear optics. However, their mechanical properties, which are crucial for practical manufacturing, processing and device durability, remain unexplored for a long period.

Thanks to the chemical variability of the extensive family of HOIPs, their mechanical properties could be well regulated using diverse A-site cations,[19–23] B-site metal ions,[24–27] or X-site linkers.[28–33] For instance, it was reported that the distinct modes of hydrogen bonding between the A-site amine cation and the anionic framework in formate HOIPs could give rise to more than 100% enhancement in elastic moduli (E) and hardness (H).[19] In addition, the ligand field stabilization energies of the B-site ions were found to be responsible for the mechanical differences in a series of isomorphous formate HOIPs $(DMA)[M(HCOO)_3]$ (DMA = dimethylammonium), where M = Mn, Co, Ni or Zn.[24] Moreover, the Jahn–Teller effect of the B-site metal ion,[25] and the electronegativity of the bridging X-site linker[28] were demonstrated to play a vital role in determining the mechanical properties of HOIPs. However, optimizing mechanical properties through the whole substitution of A-/B-/X-sites would inevitably affect other physical and chemical

---

Ordered Matter Science Research Center, Nanchang University, 330031, P. R. China. E-mail: qinyan@ncu.edu.cn; chenxg@ncu.edu.cn

† Electronic supplementary information (ESI) available: Fig. S1–S14 and Tables S1–S8. CCDC 2417523–2417525 and 2434342–2434343. For ESI and crystallographic data in CIF or other electronic format see DOI: **https://doi.org/10.1039/d5sc00620a**

‡ These authors have contributed equally to this work.

properties, which usually leads to some unexpected results. Hence, it is still a challenge to achieve giant tunability of mechanical properties through delicate chemical design and modification at the molecular level.

Reconstructive phase transitions involving cleavage and recombination of covalent bonds or coordination bonds could greatly modify materials' physical properties such as optics,[34,35] electricity,[36] mechanics,[37] and magnetism[38] without changing the chemical composition. For instance, rigid spherical C_{60} can be reconstructed into flexible two-dimensional graphene under high pressure.[39] Recently, Gao *et al.* reported that two-layer graphene can transform from sp^2 to sp^3, changing into a diamond-like structure whose films show extremely hard mechanical properties.[40] In addition, Xiong *et al.* accomplished non-destructive photo-mediated ferroelectric domains in photo-reconfigurable organic molecular materials such as Schiff bases,[41–45] diarylethene derivatives,[46–48] and fulgides,[49,50] resulting in a huge breakthrough in ferroelectric materials. In HOIPs, Shang *et al.* revealed a rare reconstructive phase transition in the hybrid formate perovskite $[CH_3CH_2NH_3][Cu(HCOO)_3]$, where a perovskite-to-diamond structural transformation is accompanied by distinct magnetic and electric ordering behaviors in the two phases.[51] Meanwhile, in CHOIPs, Xu *et al.* first achieved a bond-switching ferroelectric, forming coordination bonding between the organic cations and the inorganic cyanide framework.[5] The coordination bonds are generated in the low-temperature ferroelectric phase and broken in the high-temperature paraelectric phase, together with the order–disorder transition of cations. Similarly, Chen *et al.* designed a series of ferroelastic materials by utilizing fluorine atoms in fluorinated ligands and metals in the cyanide skeleton to form weak coordination bonds, realizing excellent dielectric switching performance and large symmetry breaking.[52,53] However, the effect of coordination bonds on the mechanical properties of HOIPs has not yet been explored.

Herein, we reported on regulating the mechanical properties using coordination bonds in CHOIP ferroelastics. By introducing a hydroxyl group onto the terminal methyl group of the organic amine in the parent $(CH_3CH_2NH_3)_2[KFe(CN)_6]$ (EA),[12] we synthesized two compounds with the same composition ($(HOCH_2CH_2NH_3)_2[KFe(CN)_6]$, EAOH) but different intermolecular interactions under different crystal growth conditions. As shown in Scheme 1, evaporation at 297 K yielded EAOH-1 with C–O–K coordination bonds, while EAOH-2 with O–H···N hydrogen-bonding interactions was obtained by evaporation at 318 K, as reported in our previous work,[12] and both of them are reddish-brown block crystals (Fig. S1, ESI†).[12] Unlike EA with weak hydrogen-bonding interactions at room temperature, hydroxyl functionalization effectively strengthens the interaction between cations and inorganic frameworks, resulting in deformation and reduced symmetry of the 3D perovskite inorganic framework, from the highly disordered cubic phase ($Fm\bar{3}m$) in EA to the ordered monoclinic phase ($P2_1/n$) in EAOH-1 and EAOH-2. Especially in EAOH-1, the C–O–K coordination bonds between hydroxyl and K^+ ions trigger cooperative displacements of K^+ and $[Fe(CN)_6]^{3-}$ units along the [101] direction, resulting in an expansion of distorted perovskite cages that can accommodate two organic cations. Further detailed crystal structure analysis shows that EAOH-1 transforms into EAOH-2 when the temperature rises to 370 K, which is unprecedented in CHOIPs. The nanoindentation experiments reveal that Young's modulus (E) and hardness (H) of EAOH-1 and EAOH-2 are enhanced compared with EA, and those of EAOH-1 show a greater increase, indicating that coordination bonds play a greater role than hydrogen-bonding interactions. This work first demonstrates the giant tunability of mechanical properties in CHOIPs by coordination bonding, which has important implications for regulating the macroscopic physical properties *via* coordination bond modulation.

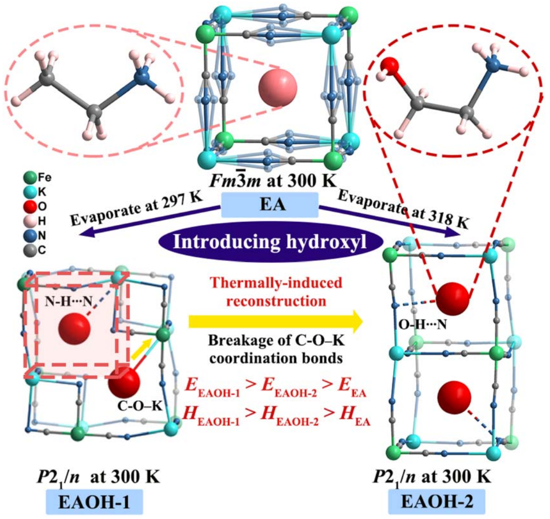

Scheme 1 Design strategy of cyanide hybrid organic–inorganic perovskite compounds EAOH-1 and EAOH-2. The smaller yellow arrow indicates the migration direction of Fe and K atoms of EAOH-1 at 300 K.

Results and discussion

Differential scanning calorimetry (DSC) and thermogravimetric analysis (TGA)

EAOH-1 shows great thermal stability up to 468 K (Fig. S2, ESI†). DSC measurements were carried out using the powder of EAOH-1 at 300–400 K under nitrogen protection. As shown in Fig. 1a, the DSC result of EAOH-1 reveals a metastable phase with distinct phase transition temperatures at 373 K upon heating and 330 K upon cooling during the first thermal cycle. This metastable behavior is absent in subsequent heating–cooling cycles. Therefore, we present a stable reversible structural phase transition of EAOH-1 at $T_c = 373/365$ K during multiple heating and cooling processes. For convenience, we define the phase below 365 K as the low-temperature phase (LTP), which only exists in the first heating process. The phase above 380 K is the high-temperature phase (HTP). The phase between 365 K and 380 K in the first heating process and below 373 K (365 K) during the second heating (cooling process) is the intermediate-temperature phase (ITP).

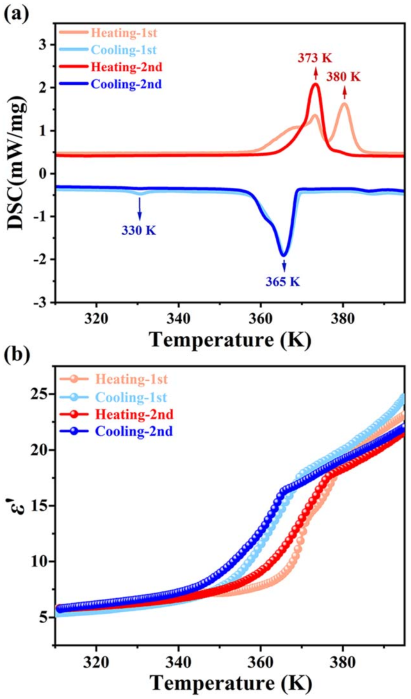

Fig. 1 (a) DSC curves of EAOH-1 in two heating–cooling cycles. (b) Temperature-dependent real part (ε′) of the dielectric constant of EAOH-1 at 1 MHz in two heating–cooling cycles.

Dielectric properties

Structural phase transitions are usually accompanied by dielectric anomalous behavior near the phase transition temperature. Temperature-dependent dielectric permittivity measurements were conducted for EAOH-1 to further verify its phase transition behavior. Fig. 1b shows that EAOH-1 exhibits apparent step-like dielectric anomalies during heating and cooling processes at 1 MHz. Similarly, during the first heating process, the dielectric anomaly exhibited two distinct steps, once again confirming the existence of the intermediate phase. During the heating process, the real part value (ε′) of the dielectric permittivity rapidly increases from 7 to 20 around T_c. The cooling process is similar to heating, with a significant thermal hysteresis at T_c. The phase transition temperature and hysteresis behavior are well consistent with the DSC results.

Raman spectroscopy

To better understand the phase transition behaviors of compound EAOH-1, a variable-temperature Raman spectroscopy experiment was performed.[54] The IR (Fig. S3, ESI†) and Raman spectra (Fig. S4, ESI†) of EA, EAOH-1, and EAOH-2 were first recorded at room temperature to demonstrate the introduction of the –OH group. The Raman vibration near 3430 cm^{-1} and the IR absorbance band from 3340–3600 cm^{-1} can be seen in EAOH-1 and EAOH-2, which proves the existence of the –OH group.[55,56] The temperature-dependent Raman spectra are displayed in Fig. S5 and S6 (ESI†), and the selected region for the lattice vibrations of EAOH-1 in the heating run is shown in Fig. 2a. Raman spectra show two transformations at about 360 and 375 K during heating, implying two successive phase transitions, consistent with the DSC results. All the observed Raman modes of EAOH-1 and EA are listed in Tables S1 and S2 (ESI†). The Raman vibrational modes reduced from seven in the LTP to five in the ITP and two in the HTP within the displayed region (Fig. 2b), indicating enhanced disorder states with increasing temperature.[57] When cooling EAOH-1 from the HTP, only one Raman transformation can be observed at about 360 K, correlating to the HTP to ITP transition. The Raman feature of the ITP is very similar to that of EAOH-2, indicating the possible irreversible transformation from EAOH-1 to EAOH-2.

Structural analyses

The variable-temperature powder X-ray diffraction (PXRD) experiment of EAOH-1 was carried out from 300 K to 400 K over a heating–cooling process. As shown in Fig. 2c and S7 (ESI†), the diffraction peaks at 300 K demonstrate the phase purity of EAOH-1. The number of peaks decreases at 365 K and 390 K, indicating the occurrence of two structural phase transitions, consistent with the DSC results. Following a heating–cooling cycle, the diffraction peaks at 313 K match well with the simulated peaks of EAOH-2 at 300 K, indicating that the transition from EAOH-1 to EAOH-2 upon heating is irreversible.

To explore the microscopic mechanism of the phase transition behaviors mentioned above, we conducted variable-temperature single-crystal X-ray diffraction experiments on EAOH-1. The corresponding crystallographic data are listed in Tables S3–S6 (ESI†). As shown in Fig. 3a and b, asymmetric units of EAOH-1 both contain two organic cations, one $[Fe(CN)_6]^{3-}$ anion, and one K^+ in the LTP and ITP. The key difference lies in how the guest cations and the host framework are connected. At 300 K (LTP), EAOH-1 crystallizes in a monoclinic space group $P2_1/n$ with unit cell parameters of a = 9.13650(10) Å, b = 11.7020(2) Å, c = 15.6616(2) Å, β = 102.6670(10)°, and V = 1633.71(4) Å^3. In Fig. 3d, one of the K atoms and Fe atoms that originally composed the $[K_4Fe_4(CN)_{12}]$ skeleton move towards the diagonal direction of the *a*-axis and *c*-axis. Such structural distortion forms an expanded pseudo-cubic coordination cage that can encapsulate two organic cations, leading to unconventional double perovskite cage structures comprising six $[KFe(CN)_3]$, in which the two ordered guest cations are located in the large cage cavity. The two adjacent $(HOCH_2CH_2NH_3)^+$ ions are linked through O–H⋯O bonds, one of which is connected to the 3D $[KFe(CN)_6]^{2-}$ framework through the C–O–K coordination bond, while the other is combined *via* O–H⋯N hydrogen-bonding interactions. Different from the high-temperature multiaxial ferroelectric $[(CH_3)_3NOH]_2[KM^{III}(CN)_6]$ with the coordination bond switching phenomenon,[4,5] where the $(CH_3)_3NOH^+$ cations all form C–O–K coordination bonds, and K^+ and Fe^{3+} ions do not exhibit significant dislocations, the unique distorted inorganic framework and cationic coordination mode of EAOH-1 in the LTP were first discovered in CHOIPs.

When the temperature rises to 368 K (ITP), compound EAOH-1 still crystallizes in $P2_1/n$, but the cell parameters become a = 11.8245(2) Å, b = 11.7157(3) Å, c = 11.9825(2) Å, β =

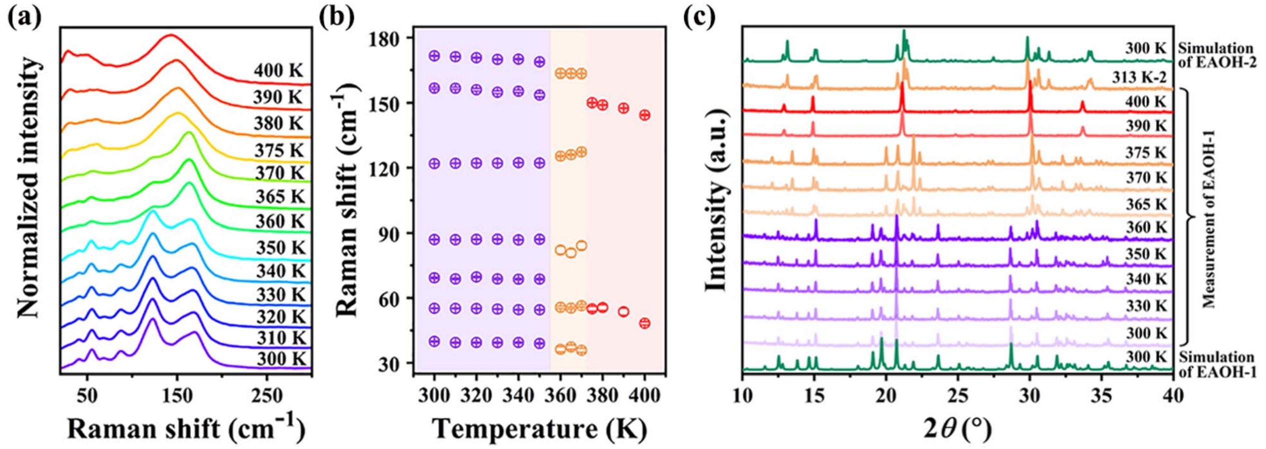

Fig. 2 (a) Selected temperature-dependent Raman spectra of EAOH-1 in the low wavenumber region on heating. (b) Temperature dependence of Raman peaks in (a) fitted with the Lorenz function. (c) The variable-temperature powder X-ray diffraction patterns of compound EAOH-1 and simulated powder X-ray diffraction patterns of compounds EAOH-1 and EAOH-2 at 300 K.

91.798(2)°, and $V = 1659.15(6)$ Å^3. The C–O–K and C–K coordination bonds are broken, and K^+ ions are connected with Fe^{3+} through CN^- linkers, resulting in a conventional cyano-bridged double perovskite structure with four $[KFe(CN)_3]$. The $(HOCH_2CH_2NH_3)^+$ cations are located in the cavity of the twisted anionic cage and connected to the framework through O–H···N bonds (Fig. 3e). The two adjacent guest cations have different configurations: one is slightly disordered with split partial occupancies refined to 0.5 : 0.5, and the other displays more disordered motion with split partial occupancies refined to 0.4 : 0.6. Moreover, the $(HOCH_2CH_2NH_3)^+$ cations are linked head-to-tail through N–H···O bonds, forming 1D supramolecular chains (Fig. S8, ESI†). The ITP of EAOH-1 has the same structure as the LTP of EAOH-2.[12] To systematically investigate

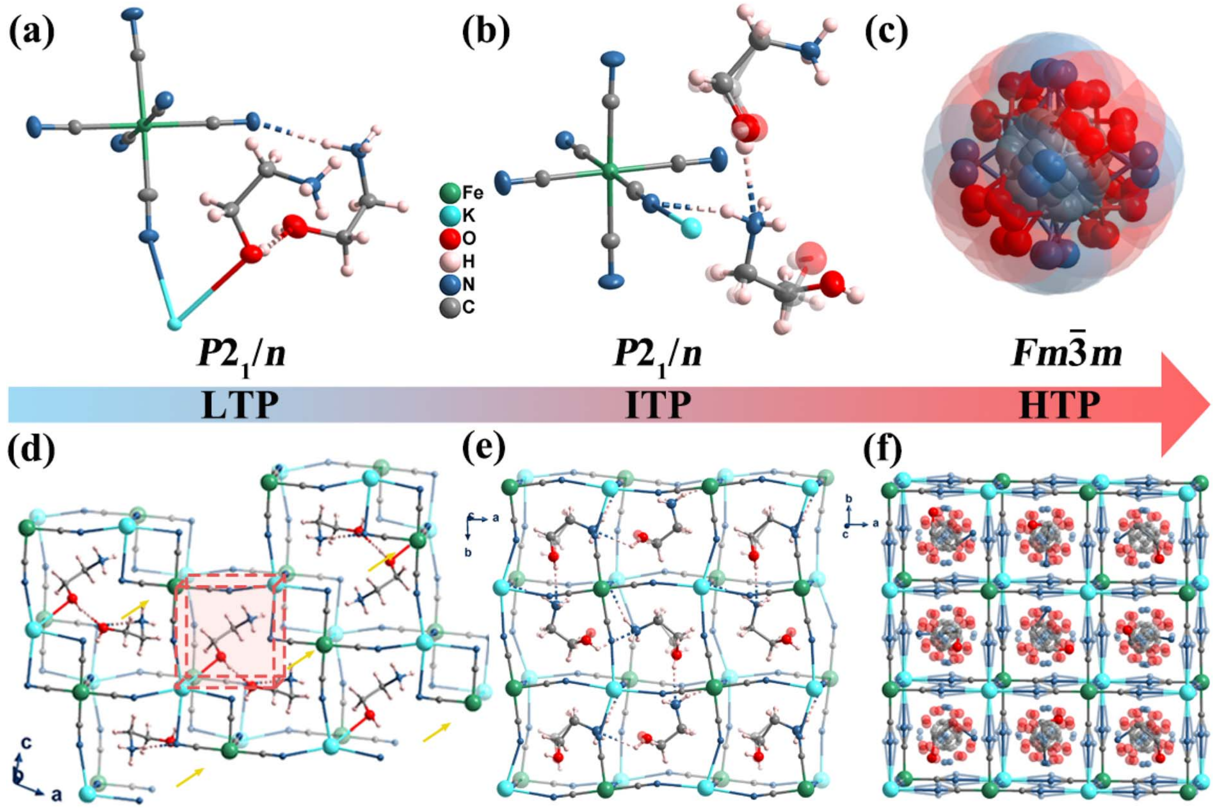

Fig. 3 The asymmetric unit of EAOH-1 in the LTP (a) and ITP (b). The corresponding cation of the HTP is amplified in (c). Perspective view of the packing structure of EAOH-1 in the LTP (d), ITP (e), and HTP (f). Partial hydrogen atoms are omitted for clarity, and the yellow arrow indicates the migration direction of Fe and K atoms in the LTP.

the irreversible reconstructive phase transition, further DSC and single-crystal X-ray diffraction analyses were conducted from 368 K to 100 K. The DSC data revealed a small exothermic peak at 303 K during the cooling process (Fig. S9, ESI†). To clarify the origin of this peak, the crystal of EAOH-1 was subsequently heated to the ITP (368 K) and the cooling process was repeated while monitoring its structure at 300 K and 100 K, respectively. Structural analysis shows that this exothermic peak arises from the cation ordering, while the 3D inorganic framework does not return to the hydroxyl-coordinated state with K^+ ions observed in the LTP of EAOH-1 (Fig. S10, ESI†).

At 388 K (phase HTP), compound EAOH-1 crystallizes in the cubic space group $Fm\bar{3}m$, with the cell parameters $a = b = c = 11.8918(7)$ Å and $V = 1681.7(3)$ Å^3. The breakdown of the O–H⋯N hydrogen bonds that connect the anion frameworks and $(HOCH_2CH_2NH_3)^+$ cations leads to a regular cubic $[KFe(CN)_6]^{2-}$ framework. The $(HOCH_2CH_2NH_3)^+$ cations present a 12-fold disorder in the cage, and the nitrogen atoms of the inorganic framework show a 4-fold disorder, achieving the high symmetry of the cubic phase (Fig. 3c and f).

In summary, compound EAOH-1 experiences the breakage and recombination of coordination bonds at 373 K during the heating process, and the connection mode between guest cations and host frames transforms from coordination bonds to hydrogen-bonding interactions. Furthermore, the order–disorder transition of the $(HOCH_2CH_2NH_3)^+$ cations and the weakening of the hydrogen-bonding interactions drive the structural phase transition at 380 K.

Ferroelastic domains

Compound EAOH-1 underwent a ferroelastic transition with an Aizu notation of $m\bar{3}mF2/m$ in the ITP and HTP, leading to 12 possible orientation states. Using polarized light microscopy on a crystal sample of EAOH-1, the evolution of ferroelastic domains was observed to further validate the ferroelasticity. As illustrated in Fig. S11 (ESI†), the chromatic attributes of EAOH-1 crystals exhibit pronounced alterations, and the emergence of stripe domains is observed on the crystal surface at 363 K, attributable to the transformation of the inorganic framework from the LTP to the ITP. Then it transformed into the ferroelastic phase with stable interlaced stripe-like ferroelastic domains at 373 K, corresponding to the ITP. Upon heating to 383 K, the ferroelastic domain patterns faded entirely in the paraelastic phase (HTP) and reoccurred gradually during the cooling process, re-entering the ITP.

Mechanical properties

Young's modulus (E) and hardness (H) are the most common and widely accepted parameters for evaluating a crystal's resistance to elastic or plastic deformation.[58] For reliable comparison, nanoindentation measurements were performed on the same crystallographic plane of (010) for EAOH-1, EAOH-2, and EA (EA is equivalent in crystallography due to the cubic phase at 300 K), as illustrated in Fig. S12 (ESI†). Fig. 4a shows the representative load–displacement curves of EAOH-1, EAOH-2 and EA. All P–h diagrams show apparent residual depths from unloading, indicating significant plastic deformation underneath the Berkovich tip. Interestingly, the required loading strengths are quite different when the targeted indentation depths are set almost the same at 400 nm. About 4 mN is required for EAOH-1 to obtain ∼400 nm indentation depth, while only 2 mN and 1.5 mN are required for EAOH-2 and EA, respectively, indicating that the stiffness of EAOH-1 is quite larger than that of EAOH-2 and EA. According to the Oliver–Pharr method,[59] E and H of EAOH-1 were calculated to be 36.68 GPa and 0.98 GPa, respectively, while E/H of EAOH-2 and EA were calculated to be 21.09/0.38 GPa and 8.82/0.26 GPa, respectively (Fig. 4d). Compared to the parent compound EA, the E and H of EAOH-1 are enhanced by approximately 300%. In comparison, EAOH-2 shows approximately a 140% increase in E and a 50% increase in H. As shown in Table S7 (ESI†), the E and H of EA and EAOH-2 are comparable to those of reported HOIPs, and those of EAOH-1 are slightly larger than those of reported HOIPs.[60–67] The dependencies of E and H on different indentation depths further support the giant enhancement of the mechanical strength of EAOH-1 (Fig. 4b and c). Notably, in comparison to the parent compound EA, the cations containing hydroxyl groups of EAOH-1 and EAOH-2 form coordination bonds and hydrogen-bonding interactions with the $[KFe(CN)_6]^{2-}$ framework, respectively. They exhibit significant differences in mechanical properties: the E and H values of EAOH-1 are larger than those of EAOH-2, and those of EAOH-2 are larger than those of EA. This indicates that the mechanical properties can be enhanced significantly by coordination bonds and hydrogen-bonding interactions, and coordination bonds play a greater role than hydrogen-bonding interactions.

To further confirm the effect of coordination bonds, we carried out variable temperature nanoindentation measurements on EAOH-1. As depicted in Fig. 4e and f and S13 (ESI†), at the same loading strength of 4 mN, the indentation depth of EAOH-1 increases from 400 nm at 295 K to 900 nm when the temperature rises to 368 K and decreases to 700 nm upon subsequent cooling to 296 K. As a result, the E and H values of EAOH-1 experience giant reductions from 32.79/0.89 GPa to 13.99/0.17 GPa for E/H, respectively, when heating from 295 to 363 K. Following cooling to 296 K, the E/H show a slight enhancement to 15.34/0.30 GPa, respectively, which are both far less than the initial values. Based on previous structural analysis, the significantly reduced stiffness and mechanical strength of EAOH-1 during heating are attributed to the structural transition from the LTP with C–O–K coordination bonds to the ITP without C–O–K coordination bonds. The unrecovered mechanical strength further confirms the irreversible phase transition upon the sequential cooling process. Consequently, the C–O–K coordination bonds of EAOH-1 are responsible for the largely stiffer and harder feature compared with EAOH-2 and EA. The suboptimal mechanical properties post-cooling, which have not reached a level comparable to those of EAOH-2 at room temperature, are likely attributable to the degradation of crystal quality following the irreversible phase transition (Fig. S14, ESI†). The overall mechanical properties of the three compounds (EA, EAOH-1, and EAOH-2) at room temperature and EAOH-1 in different phases are listed in Table S8 (ESI†).

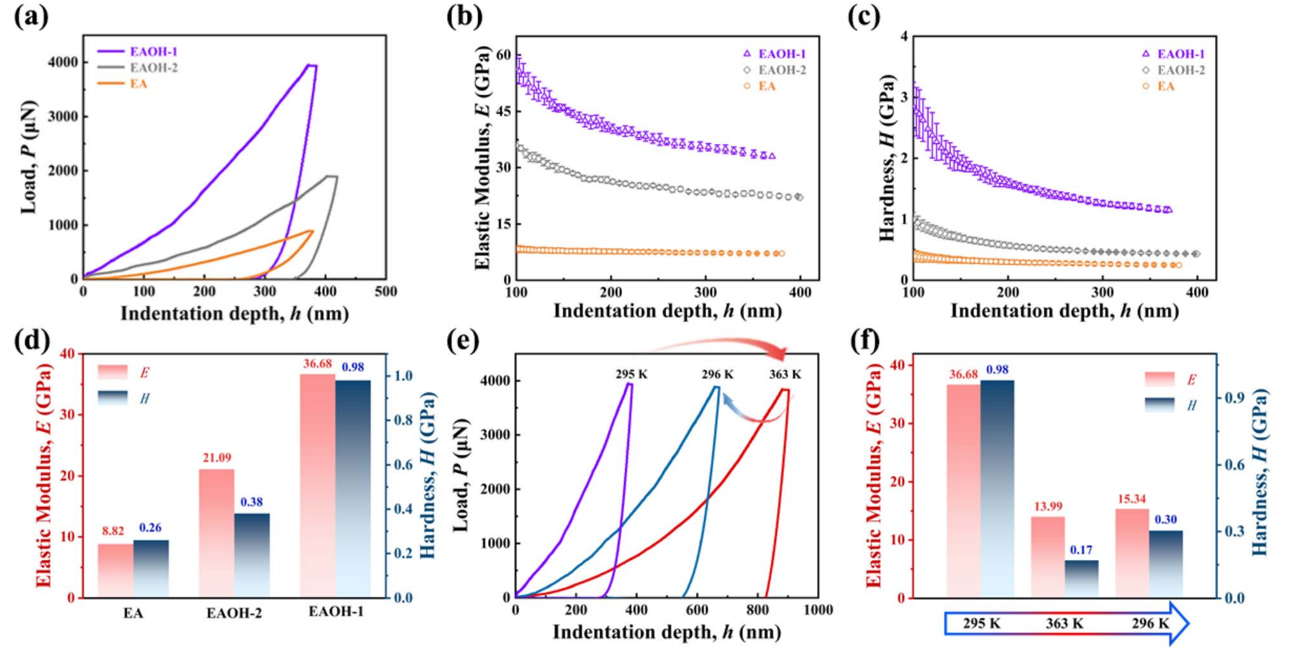

Fig. 4 Mechanical properties of EA, EAOH-1, and EAOH-2. (a) Representative load–displacement curves, (b) elastic moduli as a function of indentation depth, and (c) hardness as a function of indentation depth. (d) The histogram of the elastic moduli and hardness measured at room temperature. (e) Representative load–displacement curves and (f) elastic moduli as a function of indentation depth at different temperatures for EAOH-1.

Conclusions

In conclusion, we synthesized two isomeric $(HOCH_2CH_2NH_3)_2[KFe(CN)_6]$ (EAOH-1 and EAOH-2) crystals based on $(CH_3CH_2NH_3)_2[KFe(CN)_6]$ (EA)[12] through the hydroxyl substitution of the organic cation. EAOH-1 shows about 300% enhancements of both *E* and *H* compared to EA due to the introduced C–O–K coordination bonds, while EAOH-2 displays approximately 140% in *E* and 50% in *H* over EA due to the presence of O–H⋯N hydrogen bonding.[12] Detailed structural analysis and temperature-dependent nanoindentation measurements reveal a reconstructive phase transition from EAOH-1 to EAOH-2 due to the breaking of coordination bonds, which leads to significant reductions in mechanical strength and confirms the significant effect of coordination bonds on the mechanical properties. This study demonstrates the giant tunability of the mechanical properties of CHOIPs through intermolecular interactions, which would stimulate the regulation of the physical properties of HOIPs from a perspective of subtle chemical modification.

Data availability

The data supporting this article have been included as part of the ESI.† Crystallographic data in this study have been deposited at the CCDC under 2417523–2417525 and 2434342–2434343 and can be obtained from **https://www.ccdc.cam.ac.uk**.

Author contributions

H.-P. Lv and S.-Q. Hu contributed equally to this work. H.-P. Lv characterized and described the mechanical properties. S.-Q. Hu conceived the study and wrote the manuscript. Y.-J. Bai synthesized the samples and carried out thermal and electrical experiments. J.-S. Zhou, L.-Y. Ji, Z.-X. Wang, and Y. Ai performed the general characterization. Y. Qin guided the characterization and description of Raman spectroscopy and nanoindentation. X.-G. Chen carried out X-ray characterization and guided this work.

Conflicts of interest

The authors declare no conflict of interest.

Acknowledgements

This work was supported by the National Natural Science Foundation of China (No. 22201120, 22222502, 22405114, and 22401132), the Gan Po Juncai Support Program – the Academic and Technical Leader Training Program in Major Disciplines (20243BCE51149), and the Jiangxi Provincial Natural Science Foundation (No. 20242BAB20093 and 20242BAB20092).

Notes and references

1 C. Shi, C.-H. Yu and W. Zhang, *Angew. Chem., Int. Ed.*, 2016, **55**, 5798–5802.
2 W. Li, A. Stroppa, Z.-M. Wang and S. Gao, *Hybrid Organic-Inorganic Perovskites*, 2020, pp. 199–218, DOI: **10.1002/9783527344338.ch6**.
3 M. Rok, A. Ciżman, B. Zarychta, J. K. Zaręba, M. Trzebiatowska, M. Mączka, A. Stroppa, S. Yuan,

A. E. Phillips and G. Bator, *J. Mater. Chem. C*, 2020, **8**, 17491–17501.
4 W.-J. Xu, K. Romanyuk, Y. Zeng, A. Ushakov, V. Shur, A. Tselev, W.-X. Zhang, X.-M. Chen, A. Kholkin and J. Rocha, *J. Mater. Chem. C*, 2021, **9**, 10741–10748.
5 W.-J. Xu, P.-F. Li, Y.-Y. Tang, W.-X. Zhang, R.-G. Xiong and X.-M. Chen, *J. Am. Chem. Soc.*, 2017, **139**, 6369–6375.
6 Y. Mao, X.-G. Chen, Z.-X. Gu, Z.-X. Zhang, X.-J. Song, N. Gu and R.-G. Xiong, *Angew. Chem., Int. Ed.*, 2022, **61**, e202204135.
7 M. Rok, G. Bator, W. Medycki, M. Zamponi, S. Balčiūnas, M. Šimėnas and J. Banys, *Dalton Trans.*, 2018, **47**, 17329–17341.
8 M. Rok, G. Bator, B. Zarychta, B. Dziuk, J. Repeć, W. Medycki, M. Zamponi, G. Usevičius, M. Šimėnas and J. Banys, *Dalton Trans.*, 2019, **48**, 4190–4202.
9 M. Rok, M. Moskwa, M. Działowa, A. Bieńko, C. Rajnák, R. Boča and G. Bator, *Dalton Trans.*, 2019, **48**, 16650–16660.
10 M. Rok, M. Moskwa, A. Pawlukojć, R. Janicki, I. Zuba, P. Zieliński, P. Sobieszczyk and G. Bator, *Dalton Trans.*, 2020, **49**, 5503–5512.
11 X.-G. Chen, Z.-X. Zhang, Y.-L. Zeng, S.-Y. Tang and R.-G. Xiong, *Chem. Commun.*, 2022, **58**, 3059–3062.
12 M.-Z. Li, Z.-H. Chen, S.-Q. Hu, J.-S. Zhou, L.-Y. Ji and X.-G. Chen, *J. Mater. Chem. C*, 2023, **11**, 15952–15958.
13 W.-J. Xu, P. Zelenovskii, A. Tselev, L. Verissimo, K. Romanyuk, W. Yuan, W.-X. Zhang, A. Kholkin and J. Rocha, *Chem. Commun.*, 2023, **59**, 11264–11267.
14 W. Zhang, H.-Y. Ye, R. Graf, H. W. Spiess, Y.-F. Yao, R.-Q. Zhu and R.-G. Xiong, *J. Am. Chem. Soc.*, 2013, **135**, 5230–5233.
15 W.-J. Xu, S.-L. Chen, Z.-T. Hu, R.-B. Lin, Y.-J. Su, W.-X. Zhang and X.-M. Chen, *Dalton Trans.*, 2016, **45**, 4224–4229.
16 M. Rok, J. K. Prytys, V. Kinzhybalo and G. Bator, *Dalton Trans.*, 2017, **46**, 2322–2331.
17 M. Trzebiatowska, M. Mączka, A. Gagor and A. Sieradzki, *Inorg. Chem.*, 2020, **59**, 8855–8863.
18 M. Mączka, A. Nowok, J. K. Zareba, D. Stefańska, A. Gagor, M. Trzebiatowska and A. Sieradzki, *ACS Appl. Mater. Interfaces*, 2022, **14**, 1460–1471.
19 W. Li, A. Thirumurugan, P. T. Barton, Z. Lin, S. Henke, H. H. M. Yeung, M. T. Wharmby, E. G. Bithell, C. J. Howard and A. K. Cheetham, *J. Am. Chem. Soc.*, 2014, **136**, 7801–7804.
20 G. Kieslich, A. C. Forse, S. Sun, K. T. Butler, S. Kumagai, Y. Wu, M. R. Warren, A. Walsh, C. P. Grey and A. K. Cheetham, *Chem. Mater.*, 2016, **28**, 312–317.
21 W. Li, Z. Wang, F. Deschler, S. Gao, R. H. Friend and A. K. Cheetham, *Nat. Rev. Mater.*, 2017, **2**, 16099.
22 G. Feng, D. Gui and W. Li, *Cryst. Growth Des.*, 2018, **18**, 4890–4895.
23 L.-J. Ji, S.-J. Sun, Y. Qin, K. Li and W. Li, *Coord. Chem. Rev.*, 2019, **391**, 15–29.
24 J.-C. Tan, P. Jain and A. K. Cheetham, *Dalton Trans.*, 2012, **41**, 3949–3952.
25 D. Gui, L. Ji, A. Muhammad, W. Li, W. Cai, Y. Li, X. Li, X. Wu and P. Lu, *J. Phys. Chem. Lett.*, 2018, **9**, 751–755.
26 L.-C. An, K. Li, Z.-G. Li, S. Zhu, Q. Li, Z.-Z. Zhang, L.-J. Ji, W. Li and X.-H. Bu, *Small*, 2021, **17**, 2006021.
27 S. Grover, S. Burger, K. T. Butler, K. Hemmer, P. Vervoorts, G. Kieslich and R. Grau-Crespo, *CrystEngComm*, 2023, **25**, 3439–3444.
28 S. Sun, Y. Fang, G. Kieslich, T. J. White and A. K. Cheetham, *J. Mater. Chem. A*, 2015, **3**, 18450–18455.
29 S. Sun, F. H. Isikgor, Z. Deng, F. Wei, G. Kieslich, P. D. Bristowe, J. Ouyang and A. K. Cheetham, *ChemSusChem*, 2017, **10**, 3740–3745.
30 M. G. Ehrenreich, Z. Zeng, S. Burger, M. R. Warren, M. W. Gaultois, J.-C. Tan and G. Kieslich, *Chem. Commun.*, 2019, **55**, 3911–3914.
31 K. Li, L.-Y. Dong, H.-X. Xu, Y. Qin, Z.-G. Li, M. Azeem, W. Li and X.-H. Bu, *Mater. Chem. Front.*, 2019, **3**, 1678–1685.
32 H. Wang, H. Liu, Z. Zhang, Z. Liu, Z. Lv, T. Li, W. Ju, H. Li, X. Cai and H. Han, *npj Comput. Mater.*, 2019, **5**, 17.
33 S. Sun, S. Henke, M. T. Wharmby, H. H. M. Yeung, W. Li and A. K. Cheetham, *Inorg. Chem.*, 2015, **54**, 11186–11192.
34 I. Chung, J.-H. Song, J. Im, J. Androulakis, C. D. Malliakas, H. Li, A. J. Freeman, J. T. Kenney and M. G. Kanatzidis, *J. Am. Chem. Soc.*, 2012, **134**, 8579–8587.
35 J.-F. Lan, X. Liu, L.-X. Zhou, H.-M. Xu, W.-X. Mao, W. Sun, Y. Qin and H.-Y. Zhang, *Inorg. Chem.*, 2025, **64**, 404–411.
36 N. A. McDowell, K. S. Knight and P. Lightfoot, *Chem.–Eur. J.*, 2006, **12**, 1493–1499.
37 S. Deswal, S. K. Singh, R. Pandey, P. Nasa, D. Kabra, B. Praveenkumar, S. Ogale and R. Boomishankar, *Chem. Mater.*, 2020, **32**, 8333–8341.
38 T. Boonprab, S. J. Lee, S. G. Telfer, K. S. Murray, W. Phonsri, G. Chastanet, E. Collet, E. Trzop, G. N. L. Jameson, P. Harding and D. J. Harding, *Angew. Chem., Int. Ed.*, 2019, **58**, 11811–11815.
39 C. S. Yoo and W. J. Nellis, *SCIENCE*, 1991, **254**, 1489–1491.
40 Y. Gao, T. Cao, F. Cellini, C. Berger, W. A. de Heer, E. Tosatti, E. Riedo and A. Bongiorno, *Nat. Nanotechnol.*, 2017, **13**, 133–138.
41 Z.-X. Gu, N. Zhang, Y. Zhang, B. Liu, H.-H. Jiang, H.-M. Xu, P. Wang, Q. Jiang, R.-G. Xiong and H.-Y. Zhang, *Nat. Commun.*, 2024, **15**, 4416.
42 Z.-X. Wang, X.-G. Chen, X.-J. Song, Y.-L. Zeng, P.-F. Li, Y.-Y. Tang, W.-Q. Liao and R.-G. Xiong, *Nat. Commun.*, 2022, **13**, 2379.
43 Y.-Y. Tang, J.-C. Liu, Y.-L. Zeng, H. Peng, X.-Q. Huang, M.-J. Yang and R.-G. Xiong, *J. Am. Chem. Soc.*, 2021, **143**, 13816–13823.
44 W.-Q. Liao, B.-B. Deng, Z.-X. Wang, T.-T. Cheng, Y.-T. Hu, S.-P. Cheng and R.-G. Xiong, *Adv. Sci.*, 2021, **8**, 2102614.
45 W.-Q. Liao, Y.-L. Zeng, Y.-Y. Tang, H. Peng, J.-C. Liu and R.-G. Xiong, *J. Am. Chem. Soc.*, 2021, **143**, 21685–21693.
46 W.-Q. Liao, Y.-L. Zeng, Y.-Y. Tang, Y.-Q. Xu, X.-Y. Huang, H. Yu, H.-P. Lv, X.-G. Chen and R.-G. Xiong, *Adv. Mater.*, 2023, **35**, 2305471.
47 Y.-Y. Tang, Y.-L. Zeng and R.-G. Xiong, *J. Am. Chem. Soc.*, 2022, **144**, 8633–8640.

48 H.-Y. Zhang, N. Zhang, Y. Zhang, H.-H. Jiang, Y.-L. Zeng, S.-Y. Tang, P.-F. Li, Y.-Y. Tang and R.-G. Xiong, *Phys. Rev. Lett.*, 2023, **130**, 176802.

49 Y. Du, C.-R. Huang, Z.-K. Xu, W. Hu, P.-F. Li, R.-G. Xiong and Z.-X. Wang, *JACS Au*, 2023, **3**, 1464–1471.

50 Y. Du, W.-Q. Liao, Y. Li, C.-R. Huang, T. Gan, X.-G. Chen, H.-P. Lv, X.-J. Song, R.-G. Xiong and Z.-X. Wang, *Angew. Chem., Int. Ed.*, 2023, **62**, e202315189.

51 R. Shang, S. Chen, B.-W. Wang, Z.-M. Wang and S. Gao, *Angew. Chem., Int. Ed.*, 2016, **55**, 2097–2100.

52 S.-Q. Hu, M.-Z. Li, Z.-H. Chen, J.-S. Zhou, L.-Y. Ji, Y. Ai and X.-G. Chen, *Inorg. Chem. Front.*, 2024, **11**, 4647–4653.

53 X.-G. Chen, Z.-X. Zhang, Y.-L. Zeng, S.-Y. Tang and R.-G. Xiong, *Chem. Commun.*, 2022, **58**, 3059–3062.

54 M. Ptak, A. Sieradzki, M. Šimėnas and M. Maczka, *Coord. Chem. Rev.*, 2021, **448**, 214180.

55 M. Hajji and T. Guerfel, *J. Cluster Sci.*, 2016, **27**, 1395–1417.

56 M. Mączka, J. K. Zaręba, A. Nowok, N. Sokołowski, A. Sieradzki, A. Gągor and M. Ptak, *Chem. Mater.*, 2024, **36**, 10758–10772.

57 M. Mączka, J. K. Zaręba, A. Gągor, K. Fedoruk-Piskorska, D. Stefańska, D. Drozdowski, M. Ptak and A. Sieradzki, *ACS Appl. Mater. Interfaces*, 2024, **16**, 60564–60575.

58 D. P. Karothu, J. Mahmoud Halabi, E. Ahmed, R. Ferreira, P. R. Spackman, M. A. Spackman and P. Naumov, *Angew. Chem., Int. Ed.*, 2022, **61**, e202113988.

59 W. C. Oliver and G. M. Pharr, *J. Mater. Res.*, 1992, **7**, 1564–1583.

60 A. M. Lomonosov, X. Yan, C. Sheng, V. E. Gusev, C. Ni and Z. Shen, *Phys. Status Solidi RRL*, 2016, **10**, 606–612.

61 A. A. Mamun, Y. Mohammed, T. T. Ava, G. Namkoong and A. A. Elmustafa, *Mater. Lett.*, 2018, **229**, 167–170.

62 Q. Tu, I. Spanopoulos, E. S. Vasileiadou, X. Li, M. G. Kanatzidis, G. S. Shekhawat and V. P. Dravid, *ACS Appl. Mater. Interfaces*, 2020, **12**, 20440–20447.

63 J.-H. Lee, Z. Deng, N. C. Bristowe, P. D. Bristowe and A. K. Cheetham, *J. Mater. Chem. C*, 2018, **6**, 12252–12259.

64 K. Li, L.-Y. Dong, H.-X. Xu, Y. Qin, Z.-G. Li, M. Azeem, W. Li and X.-H. Bu, *Mater. Chem. Front.*, 2019, **3**, 1678–1685.

65 T.-M. Guo, F.-F. Gao, Z.-G. Li, Y. Liu, M.-H. Yu and W. Li, *APL Mater.*, 2020, **8**, 101106.

66 G. Feng, Y. Qin, C. Ran, L. Ji, L. Dong and W. Li, *APL Mater.*, 2018, **6**, 114201.

67 Y. Rakita, S. R. Cohen, N. K. Kedem, G. Hodes and D. Cahen, *MRS Commun.*, 2015, **5**, 623–629.